The Astrophysical Journal, 992:146 (13pp), 2025 October 10 https://doi.org/10.3847/1538-4357/ae03b6

Thermal Electrons in the Radio Afterglow of Relativistic Tidal Disruption Event ZTF22aaajecp/AT 2022cmc

Lauren Rhodes[1,2], Ben Margalit[3], Joe S. Bright[4,5], Hannah Dykaar[1,2], Rob Fender[4,6], David A. Green[7], Daryl Haggard[1,2], Assaf Horesh[8], Alexander J. van der Horst[9], Andrew K. Hughes[4], Kunal Mooley[10,11], Itai Sfaradi[12], David Titterington[7], and David Williams-Baldwin[13]
[1] Trottier Space Institute at McGill, 3550 Rue University, Montreal, QC H3A 2A7, Canada
[2] Department of Physics, McGill University, 3600 Rue University, Montreal, QC H3A 2T8, Canada
[3] School of Physics and Astronomy, University of Minnesota, Minneapolis, MN 55455, USA
[4] Astrophysics, Department of Physics, The University of Oxford, Keble Road, Oxford, OX1 3RH, UK
[5] Breakthrough Listen, Astrophysics, Department of Physics, The University of Oxford, Keble Road, Oxford, OX1 3RH, UK
[6] Department of Astronomy, University of Cape Town, Private Bag X3, Rondebosch 7701, South Africa
[7] Astrophysics Group, Cavendish Laboratory, 19 J. J. Thomson Ave., Cambridge CB3 0HE, UK
[8] Racah Institute of Physics, The Hebrew University of Jerusalem, Jerusalem 91904, Israel
[9] Department of Physics, George Washington University, 725 21st St. NW, Washington, DC 20052, USA
[10] Indian Institute Of Technology Kanpur, Kanpur, Uttar Pradesh 208016, India
[11] Caltech, 1200 E. California Blvd. MC 249-17, Pasadena, CA 91125, USA
[12] Department of Astronomy, University of California, Berkeley, CA 94720-3411, USA
[13] Jodrell Bank Centre for Astrophysics, School of Physics and Astronomy, The University of Manchester, Manchester, M13 9PL, UK
Received 2025 June 16; revised 2025 August 19; accepted 2025 September 3; published 2025 October 10

Abstract

A tidal disruption event (TDE) occurs when a star travels too close to a supermassive black hole. In some cases, accretion of the disrupted material onto the black hole launches a relativistic jet. In this paper, we present a long-term observing campaign to study the radio and submillimeter emission associated with the fifth jetted/relativistic TDE: AT 2022cmc. Our campaign reveals a long-lived counterpart. We fit three different models to our data: a nonthermal jet, a spherical outflow consisting of both thermal and nonthermal electrons, and a jet with thermal and nonthermal electrons. We find that the data are best described by a relativistic spherical outflow propagating into an environment with a density profile following $R^{-1.8}$. Comparison of AT 2022cmc to other TDEs finds agreement in the density profile of the environment but also that AT 2022cmc is twice as energetic as the other well-studied relativistic TDE, Swift J1644. Our observations of AT 2022cmc allow a thermal electron population to be inferred for the first time in a jetted transient, providing new insights into the microphysics of relativistic transients jets.

Unified Astronomy Thesaurus concepts: Tidal disruption (1696); Radio transient sources (2008); Jets (870)

1. Introduction

In a scenario where a star travels too close to a supermassive black hole (SMBH) in the center of a galaxy, the gravitational influence of the SMBH overcomes the binding energy keeping that star together and creates a tidal disruption event (TDE; M. J. Rees 1988). Roughly half of the disrupted stellar material is lost, and the rest remains gravitationally bound to the system. As the material accretes onto the central black hole, it sometimes generates and launches an outflow, which may be a relativistic jet (D. Giannios & B. D. Metzger 2011). There have been five TDEs to date interpreted as having a relativistic jet (Swift J1112.2−8238, Swift J2058.4+0516, Swift J164449.3+573451, and Arp 299-B AT1; B. A. Zauderer et al. 2011; S. B. Cenko et al. 2012; G. C. Brown et al. 2015; S. Mattila et al. 2018), the most recent of which was ZTF22aaajecp/AT 2022cmc (hereafter AT 2022cmc), the subject of this study.

AT 2022cmc was a TDE discovered by the Zwicky Transient Facility on 2022 February 11 10:42 UT (MJD 59621.4458, T_0; I. Andreoni et al. 2022a). At the time of writing, of the five confirmed relativistic TDEs, AT 2022cmc was the most distant at $z = 1.193$ (assuming $H_0 = 70\,\mathrm{km\,s^{-1}\,Mpc^{-1}}$ and $\Omega_\mathrm{M} = 0.3$; N. R. Tanvir et al. 2022). Subsequently, AT 2022cmc has been observed across the electromagnetic spectrum (I. Andreoni et al. 2022b; D. R. Pasham et al. 2023; L. Rhodes et al. 2023; T. Eftekhari et al. 2024; Y. Yao et al. 2024). The X-ray counterpart to AT 2022cmc was highly variable with large flares lasting thousands of seconds (D. R. Pasham et al. 2023) until around 400 days postdiscovery, when the X-ray flux dropped by at least an order of magnitude (T. Eftekhari et al. 2024). Radio observations covering the first 100 days postdiscovery revealed an optically thick ($\gamma \geqslant 2$, $F_\nu \propto \nu^\gamma$), evolving counterpart (I. Andreoni et al. 2022b; L. Rhodes et al. 2023). L. Rhodes et al. (2023) showed that the radio counterpart had a bulk Lorentz factor of at least 8 by studying the variability observed at 15.5 GHz, and D. R. Pasham et al. (2023) found an even higher Lorentz factor of ∼90 by applying a blazar model to the multiwavelength data. These very high Lorentz factors led investigators to conclude that there had to be a jet in the system, where the drop in X-ray flux indicated that the jet was switching off.

To explain the behavior in different wave bands, a number of different scenarios have been invoked (e.g., D. R. Pasham et al. 2023; Y. Yao et al. 2024), but in all scenarios,

nonthermal synchrotron emission drives the modeled emission. For example, I. Andreoni et al. (2022b) explained the evolving radio counterpart with synchrotron emission as is observed in gamma-ray burst (GRB) afterglows (J. Granot & R. Sari 2002). In GRB afterglow models, a highly relativistic, decelerating jet sweeps up electrons in the circumburst environment, accelerating them across a shock front into a power-law energy distribution ($N(E)\,dE \propto E^{-p}\,dE$), and then cools, emitting synchrotron emission that is brightest in the radio band (R. D. Blandford & C. F. McKee 1976; P. Mészáros & M. J. Rees 1997; R. Sari 1997; R. Sari et al. 1998). It is often, but not always, assumed that all the electrons are part of this nonthermal distribution (D. Eichler & E. Waxman 2005). The electrons cool and emit synchrotron emission that has a well-described spectrum following a number of power laws where the peak of the spectrum is optically thin and allows observers to track the electron energy distribution down to the lowest electron Lorentz factors (J. Granot & R. Sari 2002; R. A. Duncan et al. 2023). These models are valid from the regime of ultrarelativistic jets through to a nonrelativistic phase and are also used to explain Swift J1644+57, the most well-studied relativistic TDE to date.

Models have been developed that consider a thermal electron population in addition to the nonthermal population (D. Giannios & A. Spitkovsky 2009; S. M. Ressler & T. Laskar 2017; D. C. Warren et al. 2017, 2018, 2022; B. Margalit & E. Quataert 2021, 2024). Such models may be particularly important for mildly relativistic outflows where the shock velocity is $0.2 \lesssim (\Gamma\beta)_{\rm sh} \lesssim 2$ ($(\Gamma\beta)_{\rm sh}$ is the shock proper velocity), such as those produced in fast blue optical transients (A. Y. Q. Ho et al. 2022). Recent theoretical work has also explored this in the context of ultrarelativistic GRB afterglows; however, thermal electrons are typically ignored when modeling GRB observations (D. Giannios & A. Spitkovsky 2009; S. M. Ressler & T. Laskar 2017; D. C. Warren et al. 2017, 2018, 2022). The inclusion of synchrotron-emitting thermal electrons has not been explored in the modeling of TDEs.

In this paper, we present the results of a long-term radio and submillimeter monitoring campaign on the most recently discovered relativistic TDE, AT 2022cmc. In Section 2, we present the details of our monitoring campaign along with the data reduction methods used; in Sections 3 and 4, we present the results of our campaign and the different models used to explain our findings. In Section 5, we discuss the implications of these fits and contextualize them within both the TDE literature and synchrotron transients as a whole. Finally, we present our conclusions in Section 6.

2. Observations

Here, we summarize the observations and data reduction methods used to study AT 2022cmc. All the resulting flux densities and 3σ upper limits are given in Table 1. In our analysis of this source, we also include data published by I. Andreoni et al. (2022b).

2.1. Arcminute Microkelvin Imager–Large Array

The Arcminute Microkelvin Imager–Large Array (AMI-LA) is an eight-dish interferometer based in Cambridge, UK (J. T. L. Zwart et al. 2008; J. Hickish et al. 2018). It observes at a central frequency of 15.5 GHz with a bandwidth of 5 GHz, achieving an angular resolution of $\sim 30''$. While the first 100 days of observations have already been reported in L. Rhodes et al. (2023), we continued observing with AMI-LA until 2024 October. AMI-LA data are reduced using a custom software package, REDUCE_DC (Y. C. Perrott et al. 2013). Given AT 2022cmc's proximity on the sky to 3C 286, all the flux scaling and bandpass and complex gain calibration is conducted using 3C 286. Further flagging, cleaning, and deconvolution is done in CASA using the tasks *rflag*, *tfcrop*, and *tclean* (CASA Team et al. 2022).

For observations until the end of 2024 January, each observation was about 4 hr long, and the starting times, dates, and flux densities are quoted in Table 1. From 2024 February onward, as a result of the low signal-to-noise and nondetections, we concatenated multiple epochs. This was done for three sets of observations; the first included all of the observations from 2024 March, the second included those in 2024 July and August, and the final set consisted of all epochs in 2025 April. In the three stacked observations, we obtain flux densities of 0.15 ± 0.01, 0.13 ± 0.01, and 0.11 ± 0.3 mJy, respectively. These three epochs are also included in Table 1 and Figure 1.

2.2. enhanced Multi-Element Remotely Linked Interferometer Network

The *enhanced* Multi-Element Remotely Linked Interferometer Network (*e*-MERLIN) is a UK-based radio interferometer consisting of seven dishes. With a maximum baseline of 217 km, while observing at 5 GHz (*C* band and bandwidth of 0.512 GHz), *e*-MERLIN can achieve an angular resolution of $0\farcs05$. We observed AT 2022cmc with *e*-MERLIN at the *C* band between 2022 February and 2024 August for a total of nine epochs (programs RRT13002, CY16004, and CY18002; PI: L. Rhodes).

All observations were reduced using the *e*-MERLIN pipeline within CASA (J. P. McMullin et al. 2007; J. Moldon 2021). The pipeline performs preliminary flagging for radio frequency interference (RFI) and known observatory issues. Flux density scaling is performed using 3C 286 followed by bandpass calibration and complex gain calibration using OQ 208 and J1905+1943, respectively. Further flagging of the target field is conducted. We performed interactive cleaning and deconvolution using the CASA task *tclean*.

In the first two epochs, we did detect any radio emission at the coordinates of AT 2022cmc. From epoch 3 onward, we consistently detect an unresolved radio source at a position consistent with those reported in the literature.

2.3. MeerKAT

MeerKAT is a 64-dish interferometer based in the Karoo Desert, South Africa. We obtained time on MeerKAT through two open time proposals (MKT-23101 and MKT-24207; PI: L. Rhodes) to observe at both the *L* (1.28 GHz) and S4 (3.01 GHz) bands, with bandwidths of 0.875 and 0.856 GHz, respectively. In this work, we published all observations taken to date, from 2022 April until 2024 October. We plan to continue monitoring this source in future observing terms.

All MeerKAT observations were processed using `OxKAT`, a set of Python scripts specifically designed to reduce MeerKAT data (I. Heywood 2020). Each observation is first averaged

down to 1024 channels. The calibrator fields are flagged for RFI and then solved for amplitude and gain calibration solutions. The solutions are applied to the target fields, and then flagging and calibration are performed in CASA and TRICOLOUR, respectively (J. P. McMullin et al. 2007; B. V. Hugo et al. 2022). We also perform a round of phase-only self-calibration using CUBICAL[14] before imaging the field with WSCLEAN (A. R. Offringa et al. 2014).

2.4. NOrthern Extended Millimetre Array

The NOrthern Extended Millimetre Array (NOEMA), in the French Alps, monitored AT 2022cmc through programs S22BT and W22CZ (PI: L. Rhodes) between 2022 June and 2023 April. Observations were made in the 3 mm band. The data were split into two subbands (86.25 and 101.75 GHz), each with a bandwidth of 7.74 GHz.

Calibration was performed with CLIC, part of the GILDAS[15] package. For each epoch, one of the sources 3C 273, 3C 345, J1310+323, or J2200+420 was used for bandpass calibration. J1328+307, J1302−102, or J1310+323 was then used for phase and amplitude calibration. The flux densities and their errors were derived from point-source UV-plane fits to the calibrated interferometric visibilities. Given the high signal-to-noise of the detections, we were able to measure the flux density in both subbands.

3. Observational Summary

Here, we consider the basic evolution of the radio and submillimeter counterpart by examining the evolution of the spectral energy distribution (SED). Figures 1 and 2 display the data presented in Section 2 as light curves and SEDs, respectively. To describe the behavior of AT 2022cmc, we use the convention of $F_\nu \propto t^\alpha \nu^\gamma$ from 100 days postdiscovery. The light curves show that at the highest frequencies, 86.25 and 101.75 GHz (pentagons and crosses, respectively), we observe the flux density decaying with a power-law slope of $t^{-2.4\pm0.1}$. Moving to lower frequencies, in agreement with I. Andreoni et al. (2022b), a break is visible in each band. At 15.5 GHz, the peak in the light curve occurs at 300 ± 8 days, and the full 15.5 GHz light curve is well described by a broken power law with slope indices of $t^{0.33\pm0.02}$ and $t^{-2.4\pm0.1}$. There is also evidence of a tentative flattening after 1000 days.

Between 1 and 5 GHz inclusive, we obtain fewer observations, and we observe more dramatic changes in behavior. At both 3.1 and 5 GHz (squares and diamonds, respectively), the light curve appears to have a peak at ∼800 and 650 ± 40 days (we do not fit a broken power law to the 3.1 GHz data due to the low number of data points). At 5 GHz, over the first 200 days, there is variability that we cannot attribute to calibration errors. The temporal slopes follow 0.63 ± 0.07 and -1.7 ± 0.6. At 1.28 GHz, there is a rapid rise ($t^{1.6\pm0.7}$)[16] followed by a plateau ($t^{0.15\pm0.07}$).

In Figure 2, we have constructed radio and submillimeter SEDs at seven different epochs (120, 160, 270, 370, 600, 720, and 910 days) to demonstrate the spectral evolution of the radio counterpart. The peak of the SED moves from higher to lower frequencies as time progresses: between 100 and 200 days, the peak sits between 15.5 and 100 GHz, but by 900 days, it is around 3 GHz. We find that the low-frequency branch of the SED does not change with time. A joint fit to all the SEDs gives $\gamma = 1.94 \pm 0.07$ for the low-frequency branch. Conversely, the high-frequency branch becomes shallower with time. The steepest spectral index we measure is $\gamma = -3 \pm 1$ at around 370 days postdiscovery between 86.25 and 101.75 GHz, but a joint fit to all the 86.25 and 101.75 GHz (spanning 116–436 days postdiscovery) data finds a shallower spectral index of $\gamma = -1.4 \pm 0.3$. By 900 days, we measure a spectral index of $\gamma = -0.4 \pm 0.1$ between 5 and 15.5 GHz. There is a 3σ change in the high-frequency spectral index over the course of our observing campaign.

4. Modeling

In this section, we consider the wealth of radio and submillimeter observations targeting AT 2022cmc and interpret them within three different frameworks. We include the observations presented in Section 2 in addition to those published in I. Andreoni et al. (2022b) and L. Rhodes et al. (2023).

4.1. Nonthermal Relativistic Jet

L. Rhodes et al. (2023) showed that the early-time ($\lesssim$100 days) radio emission comes from an emitting region with a substantial bulk Lorentz factor ($\gtrsim$8). Hence, we first attempt to explain the radio emission using a GRB afterglow model. We compare the data at 15.5, 86.25, and 101.75 GHz (where we have the best temporal coverage) to analytical results from GRB afterglow models (J. Granot & R. Sari 2002).

At early times, a GRB jet is so relativistic that the only area visible to the observer is that within an opening angle of $1/\Gamma$ (where Γ is the bulk Lorentz factor). A jet break is an achromatic light-curve signature observed in GRB afterglows when the jet has decelerated sufficiently such that the whole shock front is visible to the observer. Both the 86.25 and 101.75 light curves follow $t^{-2.4\pm0.1}$, which is consistent with a post-jet-break light curve (t^{-p}, where p is the electron energy spectral index; R. Sari et al. 1999). The 15.5 GHz (AMI-LA) decay also follows $t^{-2.4\pm0.1}$, consistent with a jet break. The 15.5 GHz light-curve rise that follows $t^{0.33\pm0.02}$ is consistent with a GRB afterglow where the observing frequency is below the characteristic electron frequency (ν_m) and above the self-absorption frequency (ν_{sa}; A. J. van der Horst et al. 2014) in a pre-jet-break regime. In order to create a self-consistent picture, a jet break would have to occur around the same time as ν_m passing through the 15.5 GHz observing band, as only one light-curve break is observed. Without the jet break, i.e., the peak is only a result of ν_m moving through the band, we would expect the decay slope to follow $t^{-1.22\pm0.09}$. The two events occurring at the same time is not impossible but would require some fine-tuning.

This scenario also presents problems when we use closure relations from, e.g., J. Granot & R. Sari (2002) to compare the value of p from the high-frequency (15.5, 86.25, and 101.75 GHz) light curves (2.4 ± 0.1) and the high-frequency spectral index (-1.4 ± 0.3). The light curves predict $p = 2.4 \pm 0.1$ *for a post-jet-break decay* (t^{-p}), but the spectral index predicts $p = 3.8 \pm 0.6$ ($\nu^{(1-p)/2}$). The two differ at greater than 2σ. A spectral index of -0.7 is required to get

[14] https://github.com/ratt-ru/CubiCal

[15] https://www.iram.fr/IRAMFR/GILDAS

[16] We note that one of the two data points used to calculate the rise is an upper limit, and the uncertainty is calculated using the second equation in Section 2.2 from M. Espinasse & R. Fender (2018).

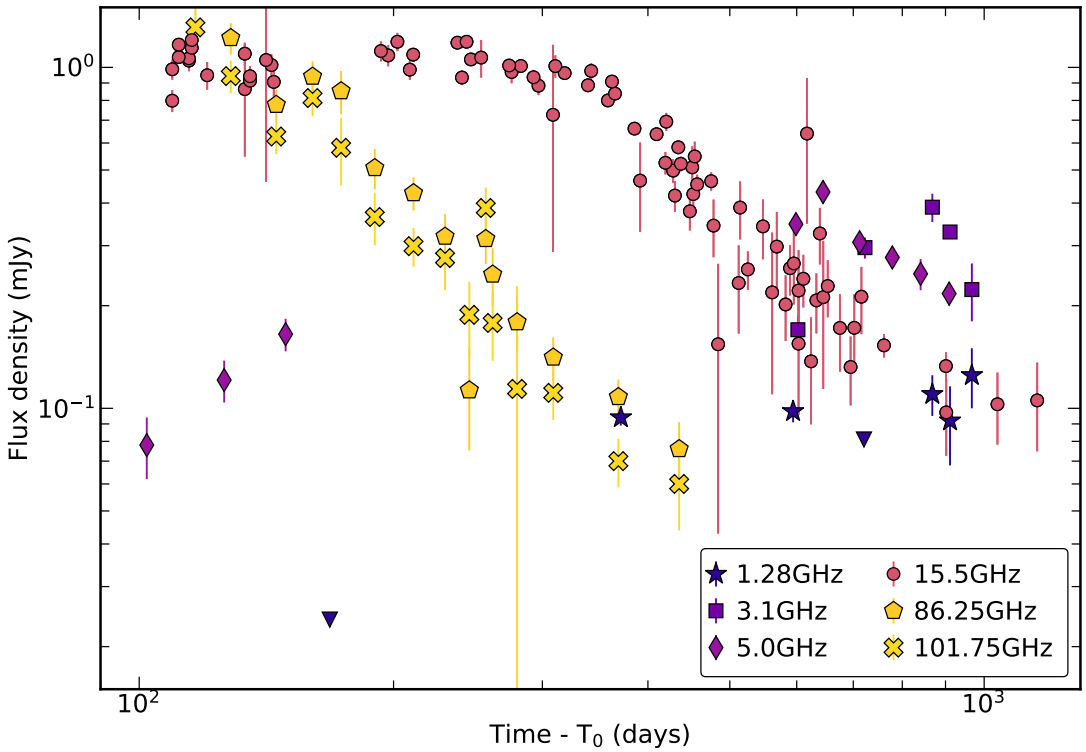

Figure 1. The radio and submillimeter light curve for AT 2022cmc between 100 and ∼1000 days postdiscovery. At the highest frequencies, 86.26 and 101.75, the light curve follows a power-law decay. At lower frequencies (15.5 GHz and below), the light curves are best described by a broken power law. We quantify the rise and decay rates at each frequency in Section 3.

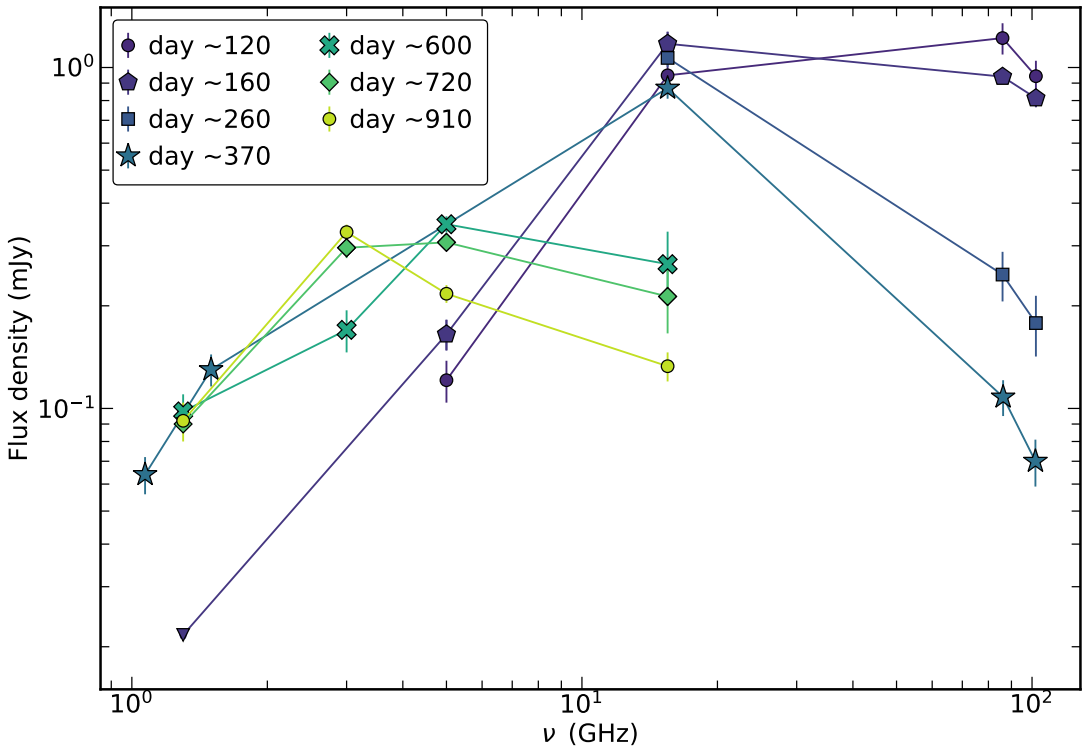

Figure 2. SEDs constructed using data in Figure 1 at 120, 160, 260, 270, 600, and 720 days postburst. There is a clear shift of the spectral peak over the duration of our campaign from above 15.5 GHz (<300 days) to around 3 GHz (∼900 days).

$p = 2.4$, which we do not measure until at least 700 days, significantly later than the time of our final NOEMA observation 370 days postdiscovery. We note that a similar issue was identified in T. Matsumoto & B. D. Metzger (2023), where the early optical spectral index was identified ($\gamma = -1.32 \pm 0.18$; I. Andreoni et al. 2022b) and attributed to

a fast cooling synchrotron scenario. Given how long we measured a steep spectral index, we find a fast cooling scenario unlikely and rule out a GRB-like scenario.

The fine-tuning required to reproduce the turnover in the 15.5 GHz light curve, combined with the discrepancy between the high-frequency decay and the spectral index, makes the GRB afterglow-like scenario difficult to reconcile with the observed radio emission from AT 2022cmc. Therefore, we rule out this interpretation.

4.2. Spherical Outflow with Thermal and Nonthermal Emitting Particles

Motivated by the steep spectral index at high frequencies, we consider the possible presence of a thermal electron population. We use the spherical outflow model presented in B. Margalit & E. Quataert (2024), an extension of B. Margalit & E. Quataert (2021), that considers any shock velocity and deceleration profile (we consider a power-law profile $(\Gamma\beta)_{\rm sh} \propto t^{-\alpha_{(\Gamma\beta)_{\rm sh}}}$), ranging from a Newtonian constant velocity scenario to an ultrarelativistic Blandford–McKee solution (R. D. Blandford & C. F. McKee 1976; R. A. Chevalier 1998). The outflow propagates into an environment parameterized by $n \propto r^{-k}$ allowing for a change in the normalization and density profile of the circumnuclear environment. Some fraction of the postshock energy is in the thermal electron population ($\epsilon_{\rm T}$), whose temperature is set by the velocity of the shock, and some fraction is carried by a nonthermal population ($\epsilon_{\rm e}$) as described in Section 4.1 (R. A. Chevalier 1998). The model calculates the emergent synchrotron luminosity considering both thermal and nonthermal electron populations, synchrotron self-absorption, and synchrotron cooling. This analytic model employs an effective line-of-sight approximation, analogous to R. Sari et al. (1998). A more detailed treatment that accurately integrates over emission from different regions of the shock (analogous to J. Granot et al. 1999a, 1999b) can only be performed numerically and is the subject of forthcoming work (R. Ferguson & B. Margalit 2025, in preparation). The overall shape of the SED and the relative contributions of the different electron populations are a strong function of the shock velocity (B. Margalit & E. Quataert 2024). The geometry of the source is assumed to be spherical. We note that this scenario is also applicable to a relativistic pre-jet-break jet, where the edges of the jet are not visible to the observer.

We fit the model described to the entire data set (I. Andreoni et al. 2022b; L. Rhodes et al. 2023) using EMCEE (D. Foreman-Mackey et al. 2013). Motivated by theory and particle-in-cell simulations, we fix the microphysical parameters and fit for the hydrodynamics of the outflow. We fix $\epsilon_{\rm T} = 0.4$ (L. Sironi et al. 2013; A. Vanthieghem et al. 2024) and $\epsilon_{\rm e} = 0.1$ in the case of a relativistic shock (L. Sironi et al. 2013; P. Beniamini & A. J. van der Horst 2017). We also fix the fraction of the energy in the magnetic fields $\epsilon_{\rm B} = 0.1$ (L. Sironi et al. 2013), which is similar to $\epsilon_{\rm e} = 0.1$ because the magnetic fields are self-amplified by the shock, and the instabilities that amplify the magnetic field would saturate once they start feeding back on the shock. This implies that the amplified magnetic field should have approximately comparable (or slightly less) energy than other components of the shock. For the parameters we fit, all had flat priors.

1. Postshock velocity $(\Gamma\beta)_{\rm sh}$ [0.0, 10.0] allowing for some power-law deceleration: $\alpha_{(\Gamma\beta)_{\rm sh}}$ [0.0, 4.0]), as well as $l_{\rm dec}$ [0.0, 8.0], which relates the instantaneous shock velocity to the shock radius.[17]
2. The number density of the environment $\log(n)$ [−3.0, 0.0]): assuming a power-law profile away from the black hole k [0.0, 4.0].
3. The nonthermal electron energy spectral index p [2.0, 3.5].

Our EMCEE run used 32 walkers and ran the chains for >10,000 steps to increase the chance of convergence. Figure 3 shows the model with the posteriors of our EMCEE run overlaid on our data alongside those from I. Andreoni et al. (2022b) and L. Rhodes et al. (2023). The top panel of Figure 3 shows the light curves at 101.75, 15.5, 5, and 1.28 GHz. The model agrees well with the shape of the 101.75, 15.5, and 5 GHz light curves. However, it struggles to match with the earliest high-frequency data and cannot recreate the lowest (1.28 GHz) light curve. The bottom panel of Figure 3 shows the SEDs at 24, 160, 370, and 910 days with the model evaluated at the same time steps. The model reproduces the observed steep spectral index at submillimeter frequencies and shows evidence for the spectrum becoming more shallow at later times. It is demonstrated more clearly here that the model tends to underpredict the flux density both at high frequencies and late times.

We find that the shock velocity follows

$$(\Gamma\beta)_{\rm sh} = 1.795^{+0.002}_{-0.003}(t/45\ {\rm days})^{-0.288\pm0.001},$$

and the number density of the circumnuclear environment has a profile with

$$n = 191 \pm 2(R/R_{45})^{-1.795^{+0.002}_{-0.003}}\ {\rm cm}^{-3},$$

where $R_{45} \approx 9.4 \times 10^{17}$ cm is the shock radius at 45 days, and we obtain a nonthermal electron spectral index of

$$p = 2.79 \pm 0.06$$

and

$$l_{\rm dec} = 1.001^{+0.003}_{-0.001},$$

where the model favors the lowest possible values of $l_{\rm dec}$.

4.3. Jetted Outflow with Thermal and Nonthermal Emitting Particles

The model presented in B. Margalit & E. Quataert (2024) considers a spherical outflow or a jetted system for which the edge of the jet is not observed. Here we build on B. Margalit & E. Quataert (2024) and consider a jet, a blast wave that starts off highly relativistic following a Blandford–McKee solution, a jet break, and then a transition into a Sedov–Taylor regime. We also consider the effect of observing the edge of the jet on the radio and submillimeter counterpart (R. Sari et al. 1999; H. Gao et al. 2013).

As with the spherical model, we used EMCEE to test the model against the data (D. Foreman-Mackey et al. 2013). The jet model is parameterized differently; in addition to p and $n \propto r^{-k}$, we fit for the jet evolution, which is dictated by the kinetic energy ($E_{\rm kin}$) adjusted for the jet's opening angle $\theta_{\rm j}$, as

[17] The lab frame radius $R = l_{\rm dec}\sqrt{1 + (\Gamma\beta)^2_{\rm sh}}\,(\Gamma\beta)_{\rm sh}c(1+z)t$, where t is the lab frame time.

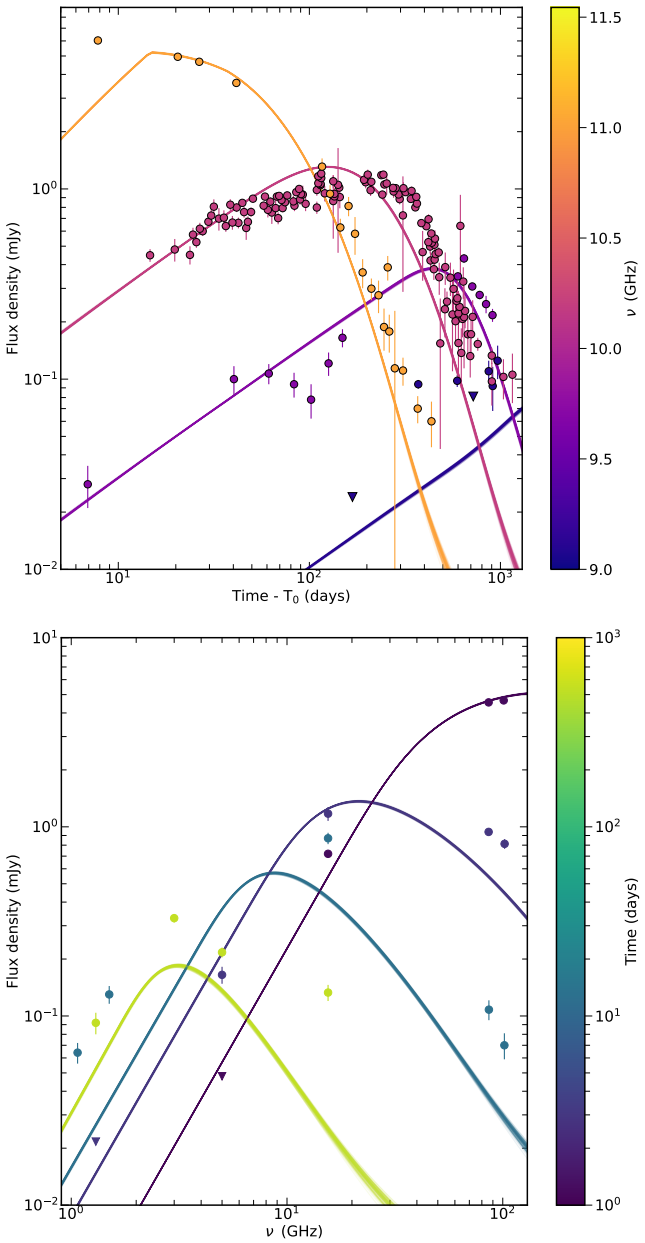

Figure 3. Top: the spherical outflow model fit (Section 4.2) to the data overlaid on the 1.28, 5, 15.5, and 101.75 GHz light curves. Bottom: the spherical outflow model fit to the data overlaid on the SEDs at ∼24, 160, 370, and 910 days postdiscovery. The model tends to underpredict the earliest high-frequency and late-time 1.28 GHz data; however, this remains our best-fit model.

well as ϵ_e, ϵ_B, and ϵ_T. We fit for the microphysical parameters because in the initial testing of fiducial values, we were not able to reproduce the rise of the light curves. We used flat priors on all parameters:

1. for the microphysical parameters $\log(\epsilon_B)$ [−6.0, 0.0], $\log(\epsilon_e)$ [−6.0, 0.0], and $\log(\epsilon_T)$ [−6.0, 0.0];
2. the isotropic equivalent kinetic energy $\log(E_{\rm kin})$ [50, 55] (erg);
3. the jet opening angle θ_j [0.0, 30] (deg);
4. the number density of the environment $\log(n)$ [−4.0, 10.0] and its profile, assuming a power-law profile away from the black hole k [0.0, 4.0], and
5. the nonthermal electron energy spectral index p [2.0, 3.5].

The results of our EMCEE run are presented in Figure 4, which shows light curves and SEDs produced by randomly sampling the posterior (post-burn-in) 100 times. The walkers in the EMCEE run struggled to converge even when they ran for $\sim 10^7$ steps. The main issue of this jet model is that the spectral evolution is not fast enough to catch the peak at each frequency. This is highlighted particularly in the top panel of Figure 4, with the peak of the 101.75 GHz light curve, which is not reproduced, and the 1.28 GHz data, where the predicted flux density is a factor of 10 off from the observed emission. We also find no change in spectral index within the model, as at all times, the high-frequency spectral index is too shallow to match the data (see the high-frequency side of the lower panel of Figure 4). Overall, comparison of the model and our data shows that an on-axis relativistic jet cannot reproduce the observed behavior.

From the jet model, we find that the kinetic energy in the jet is

$$E_K = 10^{52.5^{+0.1}_{-0.2}}\ \mathrm{erg},$$

and the density and the corresponding density profile follow

$$n = 10^{7.1^{+0.3}_{-0.4}} (R/10^{17})^{-0.02^{+0.01}_{-0.02}}\ \mathrm{cm}^{-3}.$$

The jet requires an opening angle of

$$\theta_j = 7^{+2}_{-3}{}^{\circ},$$

and the electron energy spectral index is

$$p = 2.02^{+0.02}_{-0.01},$$

which is as low as our set priors would allow. Unlike in the spherical scenario, the summation of ϵ_e, ϵ_T, and ϵ_B is less than 1 (0.8 ± 0.1):

$$\epsilon_e = 0.8 \pm 0.1,\ \epsilon_T = (3^{+3}_{-1}) \times 10^{-4},\ \epsilon_B = (2 \pm 1) \times 10^{-4}.$$

We compare the physical parameters derived from the model to other radio-detected TDEs and find that the density and profile is very different from other results in the literature (e.g., K. D. Alexander et al. 2016, 2017; T. Eftekhari et al. 2018; Y. Cendes et al. 2021a; A. J. Goodwin et al. 2024), where the density profiles of the respective circumnuclear environments fall off between r^{-1} and r^{-2} as opposed to the flat density profile with a much higher normalization.

Given the poor fit to the data and the very high densities inferred, we conclude that the radio and submillimeter emission from AT 2022cmc cannot be described by the jet model described here.

5. Discussion

Our observations of AT 2022cmc up to 1000 days postdiscovery reveal a long-lasting radio and submillimeter counterpart. The light curves in each band show a variety of behavior with steeper decays at higher frequencies (>15 GHz) than lower frequencies (1.28–5 GHz). The broadband SEDs show an optically thick ($\nu^{\sim 2}$) branch that transitions to a steep optically thin branch ($\nu^{-1.4}$). After ∼600 days, the steep optically thin spectrum becomes shallower ($\nu^{-0.7}$). Based on the steepness of the submillimeter spectral index, we infer the

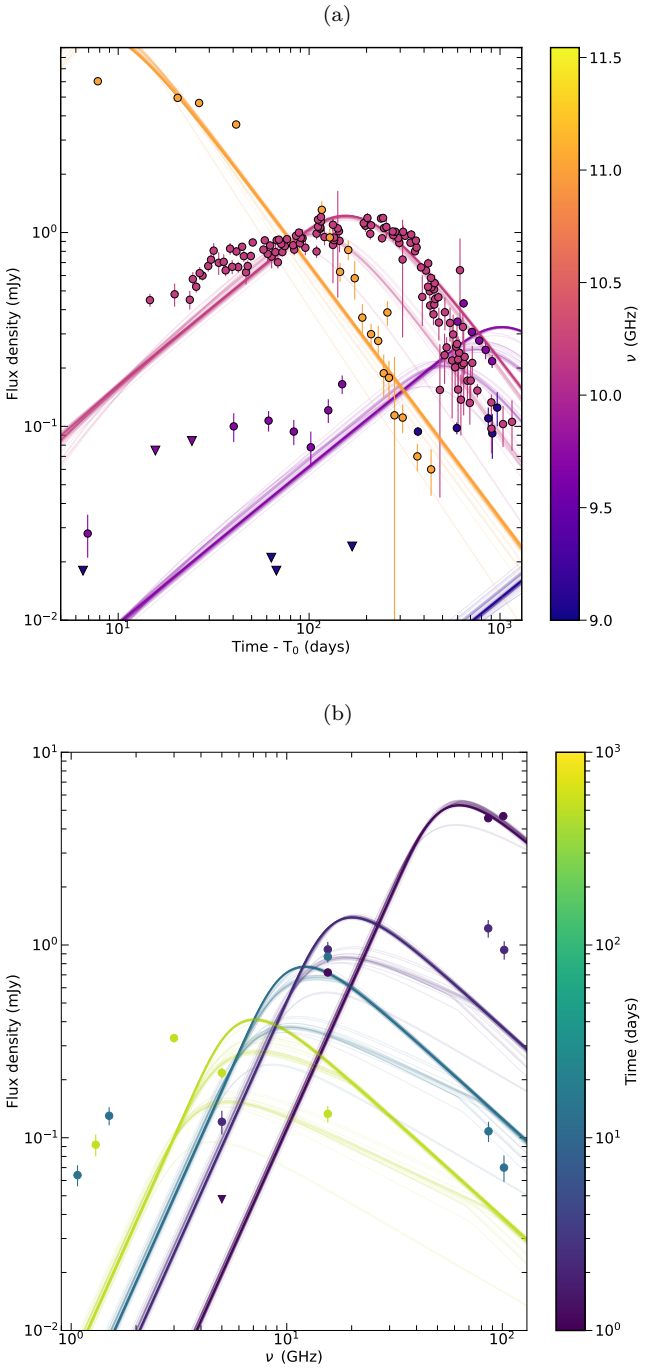

Figure 4. Top: the jetted outflow model (Section 4.3) considering both nonthermal and thermal electrons with the data overlaid on the 1.28, 5, 15.5, and 101.75 GHz light curves. Bottom: the jetted outflow model fit to the data overlaid on the SEDs. Given the scatter in the model, we only model the SEDs at ∼24, 160, 370, and 910 days postdiscovery to prevent overcluttering the figure. The jetted model cannot explain the steep spectral index, the high-frequency turnover in the first ∼10 days postdiscovery, or the low-frequency emission.

presence of a thermal electron population, in addition to a nonthermal population that begins to dominate at later times. Such a change in the spectral index over time is a hallmark expectation in models that include thermal electrons (e.g., B. Margalit & E. Quataert 2021).

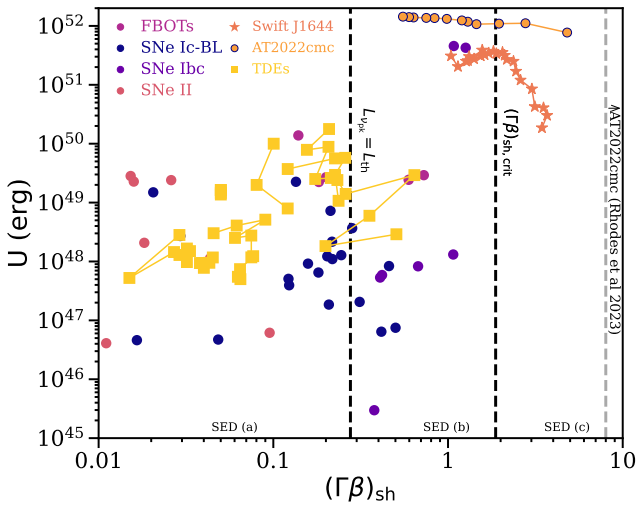

Figure 5. Postshock energy vs. shock velocity inferred from peak properties of synchrotron-powered transients including Swift J1644 and AT 2022cmc (T. Eftekhari et al. 2018; B. Margalit & E. Quataert 2024). We find that AT 2022cmc has a similar outflow velocity compared to Swift J1644 and a higher total energy content. The maximum outflow velocity we derive is not high enough to match the lower limit found in L. Rhodes et al. (2023).

5.1. Outflow Velocity and Density Profile

The shape of the SED is a strong function of the shock proper velocity $(\Gamma\beta)_{\rm sh}$ (B. Margalit & E. Quataert 2024). At the highest values of $(\Gamma\beta)_{\rm sh}$ ($\gtrsim$2), the peak of the SED is optically thin. This scenario is observed in GRB afterglows that have bulk Lorentz factors of tens to hundreds (G. Ghirlanda et al. 2018). I. Andreoni et al. (2022b) fit a series of synchrotron spectra to their radio and submillimeter SEDs spanning 5–45 days. At 11 and 20 days, they find that the peaks of the SEDs are optically thin, which according to B. Margalit & E. Quataert (2024) would require $(\Gamma\beta)_{\rm sh} > 2$, leading to possible agreement (L. Rhodes et al. 2023). At slightly lower velocities ($0.3 \lesssim (\Gamma\beta)_{\rm sh} \lesssim 2$), the SED peak becomes optically thick, and the emission is expected to be dominated by thermal electrons (if they are present), which creates a steep spectral slope just above the peak. Such a steep slope was observed in the submillimeter counterpart to AT 2022cmc until 370 days, when submillimeter observations ceased, indicating both a significant thermal electron population and that the outflow is mildly relativistic but slower than at ∼10 days (I. Andreoni et al. 2022b). We find that there is an agreement between the expected SED slope and the observed emission. At ever lower velocities ($(\Gamma\beta)_{\rm sh} \lesssim 0.3$), the peak of the SED is still optically thick but dominated by nonthermal electrons (R. A. Chevalier 1998). Above the peak frequency, the spectral index shallows, as we observed after ∼500 days. Qualitative comparison of our SEDs to those derived in different velocity regimes in B. Margalit & E. Quataert (2024) shows that there must be deceleration from an initially relativistic outflow. The fitting our model to the data finds that the outflow is decelerating $(\Gamma\beta)_{\rm sh} = 1.795(t/45\ {\rm days})^{-0.288}$ and shows the clear change in spectral index despite the later-time SEDs not being fit well by the spherical model.

Figure 5 shows the postshock energy (U) against the shock velocity ($(\Gamma\beta)_{\rm sh}$) for AT 2022cmc (from our spherical model; light orange filled circles with navy edges), thermal TDEs (gold squares), and Swift J1644 (dark orange stars) as well as

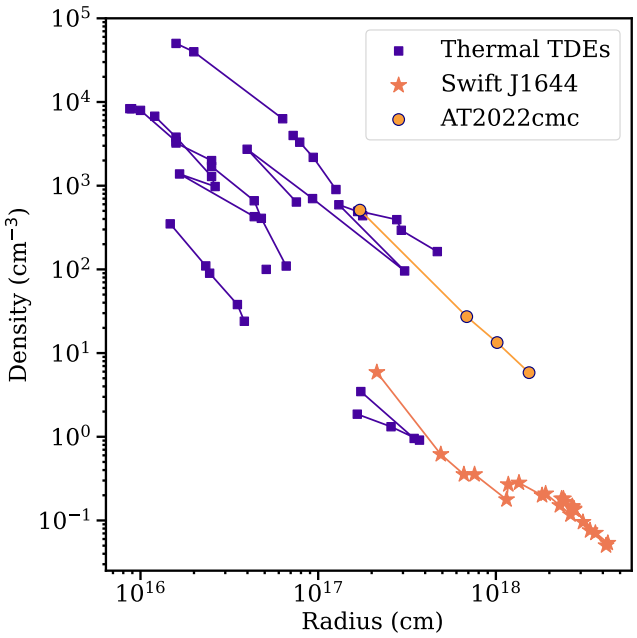

Figure 6. The number density of the circumnuclear environment as a function of distance from the SMBH for a sample of radio-detected TDEs including the other well-studied relativistic TDE, Swift J1644 (K. D. Alexander et al. 2016, 2017; T. Eftekhari et al. 2018; Y. Cendes et al. 2021a; A. J. Goodwin et al. 2022, 2023a, 2023b, 2024). Also shown is the density profile for AT 2022cmc, which shows the same density profile as the rest of the TDE population.

fast blue optical transients and three difference classes of supernovae (dark circles). The thermal TDEs sit in a lower-velocity, lower-energy region of the parameter space alongside the supernovae, away from Swift J1644 and AT 2022cmc. In terms of $(\Gamma\beta)_{\rm sh}$, Swift J1644 and AT 2022cmc fall in the same region of the parameter space. Comparison of our results to both T. Matsumoto & B. D. Metzger (2023) and Y. Yao et al. (2024) finds that we obtain marginally large proper velocity values over the same time frame. Conversely, our energy measurements for AT 2022cmc ($\sim 10^{52}$ erg) are nearly 2 orders of magnitude higher than found in Y. Yao et al. (2024), who found (3–5) $\times 10^{50}$ erg and a factor of a few lower than the isotropic equivalent energy calculated by T. Matsumoto & B. D. Metzger (2023; $\sim 9 \times 10^{52}$ erg). In the case of Y. Yao et al. (2024), we hypothesize that the difference in the total energy inferred between our study and Y. Yao et al. (2024) can be attributed to the inclusion of thermal electrons. In our spherical model, we assume $\epsilon_{\rm e} = 0.1$ and $\epsilon_{\rm T} = 0.4$, i.e., the thermal electron population has 4 times as much energy as the thermal electrons. Therefore, if only nonthermal electrons are identified and modeled, the total energy inferred will be substantially lower.

We have demonstrated both quantitatively and qualitatively from the SED that the outflow associated with AT 2022cmc is decelerating. The deceleration of the jet is dictated by the density and density profile of the environment the outflow is propagating through. A steeper density profile corresponds to a slower deceleration. Figure 6 shows the number density of the circumnuclear environment as a function of distance from the SMBH for a sample of TDEs from K. D. Alexander et al. (2016, 2017), T. Eftekhari et al. (2018), Y. Cendes et al. (2021a), and A. J. Goodwin et al. (2022, 2023a, 2023b, 2024). Overlaid is the density profile of AT 2022cmc derived from the spherical model (Section 4.2) evaluated at 24, 160, 370, and 910 days postdiscovery. We find that the density and profile of the environment that AT 2022cmc's outflow is propagating through are consistent with the rest of the TDE population. In addition, we find a similar density and profile to T. Matsumoto & B. D. Metzger's (2023) analysis of I. Andreoni et al.'s (2022b) of AT 2022cmc data, using a jet model with an opening angle of 0.1 rad. The density profile for the spherical outflow model is completely consistent ($R^{-1.795^{+0.002}_{-0.003}}$) with that seen in other TDEs ($R^{-1.5}$– R^{-2}).

It is interesting to note that the best-fit parameters inferred for the outflow deceleration $\alpha_{\Gamma\beta_{\rm sh}} \approx 0.3$ and the external density profile $k \approx 1.8$ are in rough agreement with theoretical closure relations. A spherically symmetric energy-conserving (adiabatic) blast wave expanding into a power-law density profile, $n \propto r^{-k}$, produces a shock proper velocity that depends on shock radius as $(\Gamma\beta)_{\rm sh} \propto r^{-(k-3)/2}$. This scaling is correct in both the nonrelativistic and ultrarelativistic regimes, where it correctly describes the Sedov–Taylor and Blandford–McKee solutions, respectively. These solutions are also correct for jetted or conical outflows so long as the jet does not expand laterally (i.e., accurate before the jet break time in relativistic outflows). Our model is set up assuming that the proper velocity of the shock has a power-law temporal dependence rather than a power-law dependence with radius,

$$(\Gamma\beta)_{\rm sh} \propto t^{-\alpha_{\Gamma\beta_{\rm sh}}},$$

but we note that this can be related to the shock radius, giving

$$\frac{d\ \ln(\Gamma\beta)_{\rm sh}}{d\ \ln r} = [1 - \alpha^{-1}_{(\Gamma\beta)_{\rm sh}} + (\Gamma\beta)_{\rm sh}/\sqrt{1 + (\Gamma\beta)^2_{\rm sh}}]^{-1}.$$

For an energy-conserving spherical (or conical without lateral expansion) solution as described above with $k = 1.8$ (as inferred), and for $(\Gamma\beta)_{\rm sh} \sim 1$ (relevant for most times of interest), this closure relation implies that $\alpha_{(\Gamma\beta)_{\rm sh}} \approx 0.3$, which is consistent with the inferred $\alpha_{\Gamma\beta_{\rm sh}}$ value obtained by our EMCEE fit. There is no need for this to be the case, as we did not enforce any correlation between k and $\alpha_{(\Gamma\beta)_{\rm sh}}$ in our fitting procedure, so the two parameters are formally independent in our model. The fact that the inferred parameters satisfy this closure relation therefore adds confidence in the physical plausibility of our fit. It also implies that the outflow is well within the energy-conserving phase of its hydrodynamic evolution, as opposed to being in the "ejecta-dominated" phase, where the original outflow distribution still has a significant impact (e.g., J. K. Truelove & C. F. McKee 1999).

5.2. Outflow Geometry

The jet models presented in Sections 4.1 and 4.3 are equivalent to the spherical model (Section 4.2) until the beaming angle $(1/\Gamma)$ is greater than the jet opening angle. One conclusion that can be drawn from how well the spherical model fits the observations is that if a single-component top-hat jet (one with no lateral structure) is producing all the radio and submillimeter emission, then the edges of a jet have not been observed yet. The jet would still be moving fast enough that the beaming angle of the jet is larger than $1/\Gamma$. However, as shown in Figure 5, by 900 days postdiscovery, $\Gamma\beta \sim 0.8$, which corresponds to a beaming angle of $\sim 45°$. So if a narrow jet was present, a jet break should have been visible.

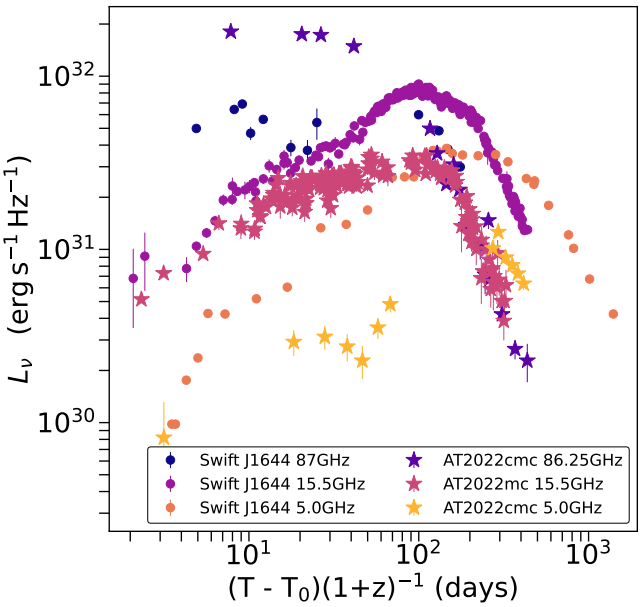

Figure 7. The 86/87, 15, and 5 GHz luminosity light curves for both AT 2022cmc and Swift J1644. While Swift J1644 is systematically more luminous than AT 2022cmc, the two events show remarkably similar light curves, but Swift J1644 has yet to be interpreted within a thermal+nonthermal scenario.

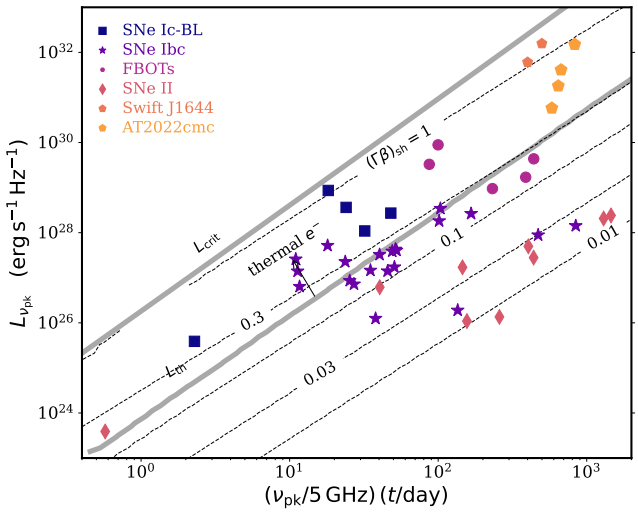

Figure 8. Radio luminosity–peak frequency parameter space plot (R. A. Chevalier 1998) recreated from Figure 2 of B. Margalit & E. Quataert (2024). The black dashed lines denote lines of constant $(\Gamma\beta)_{sh}$. The bottom gray line indicates the region above which emission at the peak frequency is dominated by thermal electrons. The top gray line labeled L_{crit} shows a theoretical upper bound for points within this parameter space (B. Margalit & E. Quataert 2024). We have plotted points corresponding to AT 2022cmc at 24, 260, 370, and 910 days.

A jet break may have been hidden in a case where there is radial structure to the outflow such that the jet does not have a traditional "top-hat" shape. C. Yuan et al. (2024) suggested that the multiwavelength emission from AT 2022cmc could be explained by a combination of a narrow, fast jet and a wider, slow jet, where each component produces its own emission signature. Lateral structure in the jet could explain not only the lack of jet break features but also the deviations between the model and data at later times. The top panel of Figure 3 shows that the model is underpredicting the 1.28 GHz light curve by a factor of 2. It maybe possible that a second component is starting to contribute to the radio SED at later times (C. Zhou et al. 2024). Continued monitoring of AT 2022cmc at centimeter wavelengths will be needed to confirm or rule out this possibility.

5.3. Comparison to Other Radio Transients

Radio observations of TDEs have allowed for a large variety of outflow properties to be inferred (K. D. Alexander et al. 2020; Y. Cendes et al. 2024; A. J. Goodwin et al. 2025). There is a wide range in luminosity and variability-timescale parameter space within which relativistic TDEs are the most radio-luminous. Within the growing sample of radio-detected TDEs, there are now a number of relativistic TDEs in the literature both on-axis and off-axis (e.g., B. A. Zauderer et al. 2011; I. Andreoni et al. 2022b; I. Sfaradi et al. 2024). However, only Swift J1644 has sufficient radio coverage on appropriate timescales for us to make detailed comparisons with AT 2022cmc.

In addition to the physical parameter comparisons that have already been made, we directly compare the observational data. Figure 7 shows the 86–87, 15.5, and 5 GHz luminosity light curves for both Swift J1644 (circles) and AT 2022cmc (stars) (E. Berger et al. 2012; B. A. Zauderer et al. 2013). Swift J1644 is systematically more luminous than AT 2022cmc for most of the observing period, but the general shape of the light curves for each event are the same at a particular frequency. We highlight two areas where there are distinct differences between the two events. First is that the high-frequency light curves of AT 2022cmc and Swift J1644 differ by a nearly a factor of 3 until the turnover at around 100 days. After this, they follow the same decay at the same luminosity, whereas at other frequencies, there is a clear offset in their luminosities. Second, we observe a rising component in the 15.5 GHz light curves. The rise in the Swift J1644 light curve has more structure, whereas the AT 2022cmc data are well described by a single power law. We highlight these two areas in particular because we find that, at least initially, they best explain the differences in the subsequent interpretations of the data.

In Swift J1644, there has been no search for a thermal electron population; instead, there have been a range of explanations including GRB-like afterglows, inverse Compton cooling, and synchrotron+synchrotron self-Compton from different emitting regions (B. D. Metzger et al. 2012; P. Kumar et al. 2013; D. Liu et al. 2015; P. Crumley et al. 2016). A thermal+nonthermal electron model has not yet been applied to the radio and submillimeter counterpart to Swift J1644. However, we note that in Y. Cendes et al. (2021b), SED modeling of the radio counterpart to Swift J1644 found that the high-frequency spectral index was quite steep, favoring $\gamma \approx -1$ ($p = 3$) when considering a nonthermal electron spectrum only. Such a steep spectrum is not unheard of in nonthermal scenarios (e.g., S. Wellons et al. 2012); however, a thermal+nonthermal scenario could also be possible. A thermal+nonthermal scenario is reinforced when examining the positions of both AT 2022cmc and Swift J1644 in Figure 8. Figure 8 shows the peak radio luminosity plotted against the product of the frequency at which the SED peaks and the time at which the SED was measured (e.g., R. A. Chevalier 1998; B. Margalit & E. Quataert 2024). The region between the two gray diagonal lines indicates the part of the parameter space where thermal electrons are expected to dominate at the peak frequency (ν_{pk}). Ignoring the contribution of the thermal electrons in this region would mean that one derives

systematically higher densities and shock velocities than when they are included. Both relativistic TDEs sit between the two thick gray lines. Therefore, one might expect other relativistic TDE systems to exhibit signatures of thermal electrons. We encourage a remodeling of the Swift J1644 data set to include thermal electrons.

5.4. Implications for Future Observing Campaigns

We have demonstrated using AT 2022cmc that submillimeter observations are vital for a better understanding of the jet physics of TDEs. The submillimeter observations give us the longest temporal baseline over which to measure the optically thin spectral index. Such a measurement is the only way to determine the relative fraction of thermal and nonthermal electrons. By combining early-time ($<$100 days) submillimeter data with late-time centimeter-wavelength data, we can measure the change in the optically thin spectral index as the jet evolves and track the transition from a thermal to nonthermal spectrum. From AT 2022cmc, we see that at early times, the thermal electrons dominate, but by the time the spectral peak reaches centimeter wavelengths, the nonthermal population dominates. Therefore, in future TDE studies, to perform the most comprehensive, physically complete modeling, submillimeter observations will be vital.

The discovery of a second relativistic TDE in real time has enabled a detailed study of the broadband emission that would otherwise not be possible and allows us to fill in more of the radio transient parameter space at the highest radio luminosities (e.g., Figure 4 of J. H. Gillanders et al. 2024). As the Vera C. Rubin Observatory comes online, the detection rate of TDEs (and hopefully relativistic TDEs) will increase by several orders of magnitude (K. Bricman & A. Gomboc 2020), providing more opportunities for submillimeter- and centimeter-wavelength follow-up and monitoring that we can use to understand the diversity in relativistic TDE parameter space.

With the launch of Einstein Probe and SVOM, the high-energy astrophysics community is now exploring a new population of jetted sources. Many of the newly discovered fast X-ray transients (FXTs; flashes of soft X-ray emission) come with optical and/or radio counterparts that sit in a similar region of luminosity/variability-timescale parameter space as both GRBs and relativistic TDEs. To fully understand the origins of FXTs and other yet-to-be-discovered high-energy transients, we need to better understand these known transients. Only then will it be possible to determine whether these new classes of transients are GRBs, relativistic TDEs, or some other type of cataclysmic event.

6. Conclusions

We have presented radio and submillimeter observations of the fifth relativistic TDE, AT 2022cmc, between 100 and 1000 days postdiscovery. Our observations show a long-lasting counterpart that corresponds to an expanding emitting region transitioning from optically thick to thin. Compared to other jetted transients, the observations presented here differ most in the postpeak spectral index. The high-frequency spectral indices we measure are relatively steep, and we test the possibility that this originates from an additional component of synchrotron-emitting thermal electrons. We test three different models against our data:

1. an entirely nonthermal GRB afterglow-like model,
2. a spherical outflow model that considers both nonthermal and thermal electrons from B. Margalit & E. Quataert (2024), and
3. a conical outflow model that considers both nonthermal and thermal electrons.

We find that the spherical outflow model provides the best fit to the data. We compare the energetics, shock velocity evolution, and circumnuclear environmental properties to that of other TDEs (Figures 5 and 6) and find that the outflow in AT 2022cmc follows a similar density profile with velocity in agreement with Swift J1644 but is more energetic by a factor of $\sim$2.

We also compare the light curve and spectral properties of AT 2022cmc and Swift J1644. Interpretations of Swift J1644 have only considered nonthermal synchrotron models, despite the clear spectral and temporal similarities between the two events. Therefore, we encourage a reanalysis of Swift J1644 within a thermal+nonthermal framework. Given their similar positions in a comparison between the radio luminosity and peak frequency (Figure 8), we expect that fitting a thermal +nonthermal electron model to the data should provide a good fit.

By identifying a thermal electron population in a jetted transient, this work has opened up a new dimension within which to study black hole jets. To date, black hole transients containing jets, such as GRBs or X-ray binaries, have considered only nonthermal electrons (parameterized through ϵ_e and ϵ_B). We have demonstrated that the shock physics in these relativistic transients is more complex but also that the observations can be interpreted using more complete models. By including thermal electrons in the modeling of future jetted transients, we will improve the accuracy of the derived physical parameters and our global understanding of these transients.

Acknowledgments

L.R. acknowledges support from the Trottier Space Institute Fellowship and the Canada Excellence Research Chair in Transient Astrophysics (CERC-2022-00009). L.R. thanks Adelle Goodwin for contributing to Figures 5 and 6. R.P.F. acknowledges support from UKRI, the ERC, and the Hintze Family Charitable Foundation. A.H. is grateful for the support by the Israel Science Foundation (ISF grant 1679/23) and by the United States–Israel Binational Science Foundation (BSF grant 2020203). This research was supported in part by grant NSF PHY-2309135 to the Kavli Institute for Theoretical Physics (KITP). D.H. acknowledges funding from the NSERC Arthur B. McDonald Fellowship and Discovery Grant programs and the Canada Research Chairs (CRC) program. The authors acknowledge support from the Centre de recherche en astrophysique du Québec, un regroupement stratégique du FRQNT.

e-MERLIN is a National Facility operated by the University of Manchester at Jodrell Bank Observatory on behalf of STFC. This project has received funding from the European Union's Horizon 2020 research and innovation program under grant agreement No. 101004719. We thank the staff at the Mullard Radio Astronomy Observatory for carrying out observations with the Arcminute Microkelvin Imager–Large Array.

Facilities: AMI, MERLIN, MeerKAT, IRAM:NOEMA.

Software: PYTHON.

Appendix
Observations

Table 1 contains all the observing dates, times, telescopes, and flux densities for our observing campaign of AT2022cmc.

Table 1
All the New Observations Reported in This Paper

Date (dd/mm/yyyy)	Time (UTC)	Telescope	Central Frequency (GHz)	Flux Density (mJy)
24/05/2022	12:45:00	*e*-MERLIN	5	0.08 ± 0.02
31/05/2022	20:57:05	AMI-LA	15.5	0.80 ± 0.07
31/05/2022	20:57:18	AMI-LA	15.5	0.99 ± 0.08
02/06/2022	19:51:22	AMI-LA	15.5	1.17 ± 0.08
02/06/2022	19:51:35	AMI-LA	15.5	1.07 ± 0.07
05/06/2022	23:01:47	AMI-LA	15.5	1.06 ± 0.09
05/06/2022	23:02:14	AMI-LA	15.5	1.05 ± 0.09
06/06/2022	20:11:19	AMI-LA	15.5	1.14 ± 0.08
06/06/2022	20:11:46	AMI-LA	15.5	1.20 ± 0.07
07/06/2022	23:55:00	NOEMA	86.25	1.6 ± 0.2
07/06/2022	23:55:00	NOEMA	101.75	1.3 ± 0.1
11/06/2022	19:17:13	AMI-LA	15.5	0.95 ± 0.1
17/06/2022	12:00:00	*e*-MERLIN	5	0.12 ± 0.02
19/06/2022	18:53:00	NOEMA	86.25	1.2 ± 0.1
19/06/2022	18:53:00	NOEMA	101.75	0.9 ± 0.1
24/06/2022	19:02:31	AMI-LA	15.5	1.1 ± 0.1
24/06/2022	19:02:59	AMI-LA	15.5	<1.0
26/06/2022	16:56:06	AMI-LA	15.5	0.91 ± 0.06
26/06/2022	16:56:27	AMI-LA	15.5	0.94 ± 0.08
02/07/2022	18:02:36	AMI-LA	15.5	<1.8
04/07/2022	19:57:56	AMI-LA	15.5	1.02 ± 0.09
05/07/2022	18:10:46	AMI-LA	15.5	0.91 ± 0.12
06/07/2022	17:25:00	NOEMA	86.25	0.78 ± 0.08
06/07/2022	17:25:00	NOEMA	101.75	0.63 ± 0.07
10/07/2022	11:30:00	*e*-MERLIN	5	0.17 ± 0.02
21/07/2022	19:56:00	NOEMA	86.25	0.9 ± 0.1
21/07/2022	19:56:00	NOEMA	101.75	0.81 ± 0.09
29/07/2022	12:59:55	MeerKAT	1.28	<0.03
03/08/2022	19:21:00	NOEMA	86.25	0.9 ± 0.1
03/08/2022	19:21:00	NOEMA	101.75	0.6 ± 0.1
20/08/2022	11:09:00	NOEMA	86.25	0.51 ± 0.07
20/08/2022	11:09:00	NOEMA	101.75	0.36 ± 0.06
23/08/2022	16:54:47	AMI-LA	15.5	1.12 ± 0.09
27/08/2022	13:28:34	AMI-LA	15.5	1.08 ± 0.09
01/09/2022	13:14:55	AMI-LA	15.5	1.19 ± 0.09
08/09/2022	11:58:30	AMI-LA	15.5	0.98 ± 0.08
10/09/2022	10:58:47	AMI-LA	15.5	1.09 ± 0.07
10/09/2022	15:03:00	NOEMA	86.25	0.43 ± 0.05
10/09/2022	15:03:00	NOEMA	101.75	0.30 ± 0.04
29/09/2022	13:46:00	NOEMA	86.25	0.32 ± 0.05
29/09/2022	13:46:00	NOEMA	101.75	0.28 ± 0.05
07/10/2022	10:50:15	AMI-LA	15.5	1.18 ± 0.07
10/10/2022	09:59:40	AMI-LA	15.5	0.93 ± 0.07
13/10/2022	11:12:38	AMI-LA	15.5	1.19 ± 0.07
15/10/2022	07:32:00	NOEMA	86.25	0.11 ± 0.04
15/10/2022	07:32:00	NOEMA	101.75	0.19 ± 0.05
16/10/2022	08:52:13	AMI-LA	15.5	1.06 ± 0.06
23/10/2022	09:17:32	AMI-LA	15.5	1.1 ± 0.2
26/10/2022	13:43:59	NOEMA	86.25	0.31 ± 0.05
26/10/2022	13:43:59	NOEMA	101.75	0.39 ± 0.06
31/10/2022	10:54:00	NOEMA	86.25	0.25 ± 0.05
31/10/2022	10:54:00	NOEMA	101.75	0.18 ± 0.04
12/11/2022	11:42:17	AMI-LA	15.5	1.01 ± 0.06
14/11/2022	08:21:57	AMI-LA	15.5	0.97 ± 0.09
18/11/2022	12:08:00	NOEMA	86.25	0.18 ± 0.03
18/11/2022	12:08:00	NOEMA	101.75	<0.3
21/11/2022	09:35:09	AMI-LA	15.5	1.01 ± 0.06
01/12/2022	07:54:00	AMI-LA	15.5	0.94 ± 0.07
05/12/2022	07:20:19	AMI-LA	15.5	0.88 ± 0.07
14/12/2022	07:02:53	AMI-LA	15.5	<1.0
17/12/2022	06:33:08	AMI-LA	15.5	<1.3
19/12/2022	06:02:28	AMI-LA	15.5	1.01 ± 0.09
27/12/2022	06:26:44	AMI-LA	15.5	0.96 ± 0.06
27/12/2022	10:11:00	NOEMA	86.25	0.14 ± 0.02
27/12/2022	10:11:00	NOEMA	101.75	0.11 ± 0.02
17/01/2023	04:31:15	AMI-LA	15.5	0.89 ± 0.06
20/01/2023	03:52:33	AMI-LA	15.5	0.98 ± 0.07
05/02/2023	02:59:36	AMI-LA	15.5	0.80 ± 0.05
09/02/2023	02:53:50	AMI-LA	15.5	0.91 ± 0.06
12/02/2023	02:49:02	AMI-LA	15.5	0.84 ± 0.06
16/02/2023	00:04:00	NOEMA	86.25	0.11 ± 0.01
16/02/2023	00:04:00	NOEMA	101.75	0.07 ± 0.01
17/02/2023	23:42:56	MeerKAT	1.28	0.09 ± 0.01
04/03/2023	01:30:23	AMI-LA	15.5	0.66 ± 0.04
10/03/2023	01:02:48	AMI-LA	15.5	0.5 ± 0.1
28/03/2023	00:25:57	AMI-LA	15.5	0.64 ± 0.04
06/04/2023	23:16:42	AMI-LA	15.5	0.52 ± 0.05
07/04/2023	23:12:47	AMI-LA	15.5	0.69 ± 0.05
15/04/2023	22:15:23	AMI-LA	15.5	0.50 ± 0.05
17/04/2023	23:45:15	AMI-LA	15.5	0.42 ± 0.05
21/04/2023	23:58:28	AMI-LA	15.5	0.58 ± 0.04
23/04/2023	21:58:00	NOEMA	86.25	0.08 ± 0.02
23/04/2023	21:58:00	NOEMA	101.75	0.06 ± 0.02
24/04/2023	23:36:11	AMI-LA	15.5	0.52 ± 0.04
05/05/2023	20:31:20	AMI-LA	15.5	0.38 ± 0.05
08/05/2023	19:37:39	AMI-LA	15.5	0.51 ± 0.08
10/05/2023	01:34:14	AMI-LA	15.5	0.43 ± 0.04
11/05/2023	20:33:10	AMI-LA	15.5	0.55 ± 0.06
14/05/2023	21:47:08	AMI-LA	15.5	0.45 ± 0.04
01/06/2023	17:36:52	AMI-LA	15.5	0.46 ± 0.04
04/06/2023	18:45:50	AMI-LA	15.5	0.34 ± 0.07
10/06/2023	18:46:11	AMI-LA	15.5	<0.3
08/07/2023	16:45:07	AMI-LA	15.5	0.23 ± 0.07
10/07/2023	17:23:08	AMI-LA	15.5	0.39 ± 0.08
21/07/2023	15:18:06	AMI-LA	15.5	0.26 ± 0.04
12/08/2023	16:22:12	AMI-LA	15.5	0.34 ± 0.07
26/08/2023	14:52:14	AMI-LA	15.5	<0.3
02/09/2023	18:02:07	AMI-LA	15.5	0.30 ± 0.08
16/09/2023	12:46:47	AMI-LA	15.5	0.20 ± 0.05
23/09/2023	13:39:13	AMI-LA	15.5	0.26 ± 0.05
28/09/2023	13:13:36	MeerKAT	1.28	0.10 ± 0.01
29/09/2023	16:43:23	AMI-LA	15.5	0.27 ± 0.07
03/10/2023	04:10:00	*e*-MERLIN	5	0.35 ± 0.02
06/10/2023	09:17:48	MeerKAT	3	0.17 ± 0.02
07/10/2023	11:32:12	AMI-LA	15.5	0.22 ± 0.07
15/10/2023	10:15:52	AMI-LA	15.5	0.24 ± 0.04
21/10/2023	11:36:00	AMI-LA	15.5	<0.9
28/10/2023	09:24:45	AMI-LA	15.5	<0.15
06/11/2023	11:57:51	AMI-LA	15.5	0.21 ± 0.04
12/11/2023	11:37:156	AMI-LA	15.5	0.33 ± 0.06
18/11/2023	11:00:41	AMI-LA	15.5	<0.3

Table 1
(Continued)

Date (dd/mm/yyyy)	Time (UTC)	Telescope	Central Frequency (GHz)	Flux Density (mJy)
18/11/2023	01:50:00	*e*-MERLIN	5	0.43 ± 0.03
26/11/2023	09:44:22	AMI-LA	15.5	0.23 ± 0.04
18/12/2023	10:10:33	AMI-LA	15.5	0.17 ± 0.04
07/01/2024	08:54:54	AMI-LA	15.5	0.13 ± 0.03
14/01/2024	09:14:15	AMI-LA	15.5	0.17 ± 0.04
24/01/2024	15:30:00	*e*-MERLIN	5	0.31 ± 0.02
28/01/2024	03:17:02	AMI-LA	15.5	0.21 ± 0.05
02/02/2024	02:37:38	MeerKAT	1.28	<0.09
04/02/2024	01:52:43	MeerKAT	3	0.30 ± 0.04
31/03/2024	00:03:20	*e*-MERLIN	5	0.28 ± 0.02
01/06/2024	11:05:00	*e*-MERLIN	5	0.25 ± 0.02
28/06/2024	16:41:25	MeerKAT	1.28	0.11 ± 0.01
28/06/2024	18:11:31	MeerKAT	3	0.39 ± 0.04
08/08/2024	11:05:00	*e*-MERLIN	5	0.22 ± 0.02
10/08/2024	13:16:30	MeerKAT	1.28	0.09 ± 0.02
10/08/2024	14:47:34	MeerKAT	3	0.33 ± 0.04
05/10/2024	09:26:25	MeerKAT	1.28	0.13 ± 0.02
05/10/2024	10:59:27	MeerKAT	3	0.22 ± 0.03
14/12/2024[a]	08:00:00	AMI-LA	15.5	0.10 ± 0.03
01/08/2024[b]	06:15:00	AMI-LA	15.5	0.10 ± 0.03
11/04/2025[c]	22:15:00	AMI-LA	15.5	0.11 ± 0.03

Note. Values in the flux density column prefaced with $<$ are 3σ upper limits. The times are the start time of each epoch. The uncertainties on the flux density are calculated by adding the statistical error on the fit and a calibration error in quadrature. For AMI-LA, NOEMA, and *e*-MERLIN, we use a calibration error of 5%, and for MeerKAT, we use 10%. For the concatenated data sets, we provide the central time as opposed to the observing start time.
[a] The results of concatenating the data collected in 2024 March.
[b] The results of concatenating the data collected in 2024 July and August.
[c] The results of concatenating the data collected in 2025 April.

ORCID iDs

Lauren Rhodes https://orcid.org/0000-0003-2705-4941
Ben Margalit https://orcid.org/0000-0001-8405-2649
Joe S. Bright https://orcid.org/0000-0002-7735-5796
Hannah Dykaar https://orcid.org/0009-0008-6396-0849
David A. Green https://orcid.org/0000-0003-3189-9998
Daryl Haggard https://orcid.org/0000-0001-6803-2138
Assaf Horesh https://orcid.org/0000-0002-5936-1156
Alexander J. van der Horst https://orcid.org/0000-0001-9149-6707
Andrew K. Hughes https://orcid.org/0000-0003-0764-0687
Kunal Mooley https://orcid.org/0000-0002-2557-5180
Itai Sfaradi https://orcid.org/0000-0003-0466-3779
David Titterington https://orcid.org/0000-0003-1431-920X
David Williams-Baldwin https://orcid.org/0000-0001-7361-0246

References

Alexander, K. D., Berger, E., Guillochon, J., Zauderer, B. A., & Williams, P. K. G. 2016, ApJL, 819, L25
Alexander, K. D., van Velzen, S., Horesh, A., & Zauderer, B. A. 2020, SSRv, 216, 81
Alexander, K. D., Wieringa, M. H., Berger, E., Saxton, R. D., & Komossa, S. 2017, ApJ, 837, 153
Andreoni, I., Coughlin, M., Ahumada, T., et al. 2022a, TNSAN, 38, 1
Andreoni, I., Coughlin, M. W., Perley, D. A., et al. 2022b, Natur, 612, 430
Beniamini, P., & van der Horst, A. J. 2017, MNRAS, 472, 3161
Berger, E., Zauderer, A., Pooley, G. G., et al. 2012, ApJ, 748, 36
Blandford, R. D., & McKee, C. F. 1976, PhFl, 19, 1130
Bricman, K., & Gomboc, A. 2020, ApJ, 890, 73
Brown, G. C., Levan, A. J., Stanway, E. R., et al. 2015, MNRAS, 452, 4297
CASA Team, Bean, B., Bhatnagar, S., et al. 2022, PASP, 134, 114501
Cendes, Y., Alexander, K. D., Berger, E., et al. 2021a, ApJ, 919, 127
Cendes, Y., Berger, E., Alexander, K. D., et al. 2024, ApJ, 971, 185
Cendes, Y., Eftekhari, T., Berger, E., & Polisensky, E. 2021b, ApJ, 908, 125
Cenko, S. B., Krimm, H. A., Horesh, A., et al. 2012, ApJ, 753, 77
Chevalier, R. A. 1998, ApJ, 499, 810
Crumley, P., Lu, W., Santana, R., et al. 2016, MNRAS, 460, 396
Duncan, R. A., van der Horst, A. J., & Beniamini, P. 2023, MNRAS, 518, 1522
Eftekhari, T., Berger, E., Zauderer, B. A., Margutti, R., & Alexander, K. D. 2018, ApJ, 854, 86
Eftekhari, T., Tchekhovskoy, A., Alexander, K. D., et al. 2024, ApJ, 974, 149
Eichler, D., & Waxman, E. 2005, ApJ, 627, 861
Espinasse, M., & Fender, R. 2018, MNRAS, 473, 4122
Foreman-Mackey, D., Hogg, D. W., Lang, D., & Goodman, J. 2013, PASP, 125, 306
Gao, H., Lei, W.-H., Zou, Y.-C., Wu, X.-F., & Zhang, B. 2013, NewAR, 57, 141
Ghirlanda, G., Nappo, F., Ghisellini, G., et al. 2018, A&A, 609, A112
Giannios, D., & Metzger, B. D. 2011, MNRAS, 416, 2102
Giannios, D., & Spitkovsky, A. 2009, MNRAS, 400, 330
Gillanders, J. H., Rhodes, L., Srivastav, S., et al. 2024, ApJL, 969, L14
Goodwin, A. J., Alexander, K. D., Miller-Jones, J. C. A., et al. 2023a, MNRAS, 522, 5084
Goodwin, A. J., Anderson, G. E., Miller-Jones, J. C. A., et al. 2024, MNRAS, 528, 7123
Goodwin, A. J., Burn, M., Anderson, G. E., et al. 2025, ApJS, 278, 36
Goodwin, A. J., Miller-Jones, J. C. A., van Velzen, S., et al. 2023b, MNRAS, 518, 847
Goodwin, A. J., van Velzen, S., Miller-Jones, J. C. A., et al. 2022, MNRAS, 511, 5328
Granot, J., Piran, T., & Sari, R. 1999a, ApJ, 513, 679
Granot, J., Piran, T., & Sari, R. 1999b, ApJ, 527, 236
Granot, J., & Sari, R. 2002, ApJ, 568, 820
Heywood, I. 2020, oxkat: Semi-automated Imaging of MeerKAT Observations, Astrophysics Source Code Library, ascl:2009.003
Hickish, J., Razavi-Ghods, N., Perrott, Y. C., et al. 2018, MNRAS, 475, 5677
Ho, A. Y. Q., Margalit, B., Bremer, M., et al. 2022, ApJ, 932, 116
Hugo, B. V., Perkins, S., Merry, B., Mauch, T., & Smirnov, O. M. 2022, in ASP Conf. Ser. 532, Astronomical Data Analysis Software and Systems XXX, ed. J. E. Ruiz, F. Pierfedereci, & P. Teuben (San Francisco, CA: ASP), 541
Kumar, P., Barniol Duran, R., Bošnjak, Ž., & Piran, T. 2013, MNRAS, 434, 3078
Liu, D., Pe'er, A., & Loeb, A. 2015, ApJ, 798, 13
Margalit, B., & Quataert, E. 2021, ApJL, 923, L14
Margalit, B., & Quataert, E. 2024, ApJ, 977, 134
Matsumoto, T., & Metzger, B. D. 2023, MNRAS, 522, 4028
Mattila, S., Pérez-Torres, M., Efstathiou, A., et al. 2018, Sci, 361, 482
McMullin, J. P., Waters, B., Schiebel, D., Young, W., & Golap, K. 2007, in ASP Conf. Ser. 376, Astronomical Data Analysis Software and Systems XVI, ed. R. A. Shaw, F. Hill, & D. J. Bell (San Francisco, CA: ASP), 127
Mészáros, P., & Rees, M. J. 1997, ApJ, 476, 232
Metzger, B. D., Giannios, D., & Mimica, P. 2012, MNRAS, 420, 3528
Moldon, J. 2021, e-MERLIN CASA Pipeline, Astrophysics Source Code Library, ascl:2109.006
Offringa, A. R., McKinley, B., Hurley-Walker, N., et al. 2014, MNRAS, 444, 606
Pasham, D. R., Lucchini, M., Laskar, T., et al. 2023, NatAs, 7, 88
Perrott, Y. C., Scaife, A. M. M., Green, D. A., et al. 2013, MNRAS, 429, 3330
Rees, M. J. 1988, Natur, 333, 523
Ressler, S. M., & Laskar, T. 2017, ApJ, 845, 150
Rhodes, L., Bright, J. S., Fender, R., et al. 2023, MNRAS, 521, 389
Sari, R. 1997, ApJL, 489, L37
Sari, R., Piran, T., & Halpern, J. P. 1999, ApJL, 519, L17
Sari, R., Piran, T., & Narayan, R. 1998, ApJL, 497, L17

Sfaradi, I., Beniamini, P., Horesh, A., et al. 2024, MNRAS, 527, 7672
Sironi, L., Spitkovsky, A., & Arons, J. 2013, ApJ, 771, 54
Tanvir, N. R., de Ugarte Postigo, A., Izzo, L., et al. 2022, GCN, 31602, 1
Truelove, J. K., & McKee, C. F. 1999, ApJS, 120, 299
van der Horst, A. J., Paragi, Z., de Bruyn, A. G., et al. 2014, MNRAS, 444, 3151
Vanthieghem, A., Tsiolis, V., Spitkovsky, A., et al. 2024, PhRvL, 132, 265201
Warren, D. C., Barkov, M. V., Ito, H., Nagataki, S., & Laskar, T. 2018, MNRAS, 480, 4060
Warren, D. C., Dainotti, M., Barkov, M. V., et al. 2022, ApJ, 924, 40
Warren, D. C., Ellison, D. C., Barkov, M. V., & Nagataki, S. 2017, ApJ, 835, 248
Wellons, S., Soderberg, A. M., & Chevalier, R. A. 2012, ApJ, 752, 17
Yao, Y., Lu, W., Harrison, F., et al. 2024, ApJ, 965, 39
Yuan, C., Zhang, B. T., Winter, W., & Murase, K. 2024, ApJ, 974, 162
Zauderer, B. A., Berger, E., Margutti, R., et al. 2013, ApJ, 767, 152
Zauderer, B. A., Berger, E., Soderberg, A. M., et al. 2011, Natur, 476, 425
Zhou, C., Zhu, Z.-P., Lei, W.-H., et al. 2024, ApJ, 963, 66
Zwart, J. T. L., Barker, R. W., Biddulph, P., et al. 2008, MNRAS, 391, 1545